Experimental model updating of slope considering spatially varying soil properties and dynamic loading

Ruohan Wang[a,b,*], Jiayi Ouyang[b,c], Vasileios C. Fragkoulis[d], Yong Liu[b], Michael Beer[a,e,f]

[a] *Institute for Risk and Reliability Leibniz University Hannover 30167 Hannover Germany*
[b] *State Key Laboratory of Water Resources Engineering and Management Wuhan University 430072 China*
[c] *China Three Gorges Construction Engineering Corporation Chengdu 610041 Sichuan China*
[d] *Department of Civil and Environmental Engineering University of Liverpool Liverpool L69 3GH UK*
[e] *Institute for Risk and Uncertainty and School of Engineering University of Liverpool Liverpool L69 7ZF UK*
[f] *International Joint Research Center for Resilient Infrastructure & International Joint Research Center for Engineering Reliability and Stochastic Mechanics Tongji University Shanghai 200092 China*

Abstract

The widespread threat posed by slope structure failures to human lives and property safety is widely acknowledged. Additionally, natural soil often displays spatial variability due to geological deposition and other factors. Therefore, predicting the seismic response of slopes subjected to ground motions and inversely analyzing the spatial distribution of soils remains an unresolved issue. In the present work, a shaking table experimental test is first designed and carried out, in which a soft-soil slope dynamic system is established. To capture the seismic response of the soft-soil slope, specifically the experimental characteristic of acceleration and soil pressure response in both spatial domain and time domain, a series of sensors were pre-embedded in the slope. Subsequently, a model updating approach is proposed for slope seismic analysis that incorporates spatial variability of soil. In addition, to enhance computational efficiency, the dimensionality reduction of Karhunen-Loève expansion method is introduced to reduce inverse analysis parameters. Based on 34 samples collected from experimental data, it is shown that near-fault pulse-like ground motions deliver greater concentrated energy, causing more severe damage to slope structures, especially the topsoil layer. Furthermore, using data obtained from a shaking table test subjected to ground motion RSN 158H1 from the PEER NGA-West2 database as an example, it is also shown that the proposed approach demonstrates high accuracy in predicting the spatial distribution of the maximum shear modulus in soil slope dynamic systems. The present work

---

*corresponding author

Email addresses: `ruohan.wang@irz.uni-hannover.de` (Ruohan Wang), `ouyangjy@whu.edu.cn` (Jiayi Ouyang), `vasileios.fragkoulis@liverpool.ac.uk` (Vasileios C. Fragkoulis), `liuy203@whu.edu.cn` (Yong Liu), `beer@irz.uni-hannover.de` (Michael Beer)

not only addresses the challenges posed by mainshock-aftershock effects but also highlights the potential of model updating approaches to enhance the understanding of slope behavior under seismic loading conditions.

Keywords: Shaking table test, Model updating, Bayesian analysis, Markov chain Monte Carlo, Seismic hazard

1. Introduction

Landslides triggered by earthquakes have caused significant damage and loss of life around the world. Understanding the mechanisms and evaluating seismic responses that contribute to earthquake-induced landslides is critical for mitigating their impacts and reducing the risk of future disasters [1, 2, 3]. In fact, earthquakes often constitute a continuous process, wherein a mainshock is usually followed by a series of aftershocks [4, 5]. Additionally, regions within the same seismic zone frequently experience multiple earthquake events. Subjected to the influence of multiple earthquake events, slope structures previously damaged by the seismic excitation may be incapable of withstanding the impact of the next seismic event, potentially resulting in complete failure [6]. This vulnerability is particularly pronounced in the case of soft-soil slopes, where the seismic amplification effect of the soft soil can significantly amplify cumulative damage [7, 8]. Therefore, predicting the seismic responses caused by seismic excitations is critical for the safety of structures. However, the majority of studies have focused on the effects of multiple earthquake events mostly for steel structures, wood structures, single-degree-of-freedom systems, etc. There is a significant scarcity of research concerning the damage to slope structures under seismic excitations.

Currently, ground motions can be primarily classified into two categories based on the presence of pulses; these are pulse-like ground motion (PLGM) and non-pulse ground motion (NPGM). However, near-fault pulse-like ground motions that feature a long-period and high-amplitude pulse in velocity signal potentially cause more severe damage. Some studies have already been done in this area including topics such as generation principle [9], identification [10], numerical simulation [11], and impacts on structures [12, 13]. Nonetheless, despite attempts to quantify the impacts of PLGMs and NPGMs on actual slope structures through numerical simulations, the understanding of this critical issue remains unclear. In this context, the objective is to derive evolving rules under different seismic excitations. This is crucial for a better understanding of slope failure mechanisms, providing the foundation for improving numerical models. Achieving this goal necessitates the implementation of relevant experimental studies. As for experimental study, Bao et al. [14] investigated the effect of near-fault ground motions with disparate intensities; Bao et al. [15] also examined the influence of PLGMs but, in general, additional research effort should be put towards the exploration of the seismic response of soft-soil slope dynamic systems under PLGMs and NPGMs.

In terms of the relevant numerical analysis, the response and reliability of slope structures subjected to seismic ground motions have consistently been a topic of interest among scholars. In the analysis of slope dynamic reliability, it is important to note that the majority of existing assessment models are built upon the Newmark-type procedure (e.g. [16, 17, 18]). In comparison to the latter, numerical stress-strain analysis can often offer more precise estimations of the dynamic behavior of slope systems [19, 20]. Moreover, in current numerical-based research, it is commonly assumed that soil properties within the soil strata are uniform, and the uncertainty associated with soil parameter variations is often simply disregarded. The inherent spatial variability of soil characteristic parameters has not yet been incorporated into the current probability-based numerical methods [21, 22]. In reality, this spatial variability of soil composition often exhibits significant variations spanning several orders of magnitude, which can indeed impart certain influences on the analysis outcomes [23, 24, 25]. The potential impact of non-uniform soil properties on seismic hazards in slope dynamic systems remains uncertain. However, the spatial distribution field of soils in actual site is typically unknown. Therefore, determining how to inversely analyze the spatial distribution field of soil properties in the investigation site is critical.

In this context, adopting a model updating approach can well address the above issues. In geotechnical engineering, predictions of slope models often differ significantly from the measured results. Thus, the model updating approach can assist engineers in calibrating geotechnical material parameters or numerical models by incorporating test data, monitoring data, and field observation data [26, 27, 28]. Bayesian methods stand out as a frequently employed strategy in model updating, providing a probabilistic perspective to address the challenges of refining models [29, 30, 31]. The most common method of Bayesian updating is carried out through sampling techniques, such as Markov chain Monte Carlo (MCMC) methods. Uribe et al. [32] explored how varying the prior random field model influences the resolution of Bayesian inverse problems. However, incorporating the spatial variability of the soil into Bayesian updating introduces a significant increase in parameter dimensions, increasing, subsequently, the associated computational cost [33]. Conventional Bayesian methods often struggle to effectively address this issue [34]; especially, maintaining the stationarity and achieving convergence of Markov chains in high-dimensional spaces presents a formidable challenge [35]. The intricacy of Bayesian updating tends to increase when handling discrete outputs in high-dimensional spaces. This, in turn, results in a heavy computational burden for likelihood function evaluations [33]. In such cases, due to the curse of dimensionality in both modeling and simulation, even efficient surrogate model methods may fail to achieve their anticipated potential. Hence, the present study introduces the integration of K-L dimensionality reduction techniques into the framework for discrete processes, enabling the use of low-dimensional models to reduce the associated computational costs.

In this paper, aiming at addressing the aforementioned challenges, a shaking table experimental test is first designed and carried out, in which a soil slope dynamic system is established. To capture the seismic response of a soft-soil slope dynamic system, particularly the experimental characteristics of acceleration, stability, and residual deformation, a series of sensors are pre-embedded in the slope to acquire 34 sets of data samples. Subsequently, a real-time model-updating-based adaptive approach is proposed, which incorporates soil spatial variability and introduces the concept of dimensionality reduction for K-L expansion method for geotechnical structures subjected to sequential seismic motions. By doing so, the herein proposed approach accurately predicts the potential seismic responses of soil structures and inversely analyzes the spatial distribution field of real-site soil parameters. Finally, the feasibility of the proposed approach is validated through the analysis of a soft-soil slope, coupled with the acquired data from shaking table tests.

2. Experimental setup

2.1. Shaking table test

Influenced by the Honghe fault zone, Honghe Autonomous Prefecture of Yunnan Province, China, and its surrounding areas have been severely affected by historical earthquakes leading to landslides and loss of property [36]. In the present study, red clay soil which is used as test soil was obtained from the Duodi Village, Honghe Autonomous Prefecture, Yunnan Province [37, 38]. Taking into account that particle size composition is an important indicator for determining soil type, the herein used particle size composition is characterized by Bettersize 2600 laser particle size analyzer. The detection principle of the machine is to use a monochromatic laser of a certain wavelength as a light source. The spatial distribution of the diffracted and scattered light energy is only related to the particle size, so that the particle size distribution (PSD) curve of the soil is obtained (e.g. [39, 40, 41]). Moreover, the measuring range of the analyzer is lies in the range of 0.02-2600 μm and contains 100 particle size classes. The PSD curve of the test soil is shown in Figure 1. The PSD curve indicates that the particle diameters of the tested soil samples fall within the range of clay where the diameter is less than 75 μm.

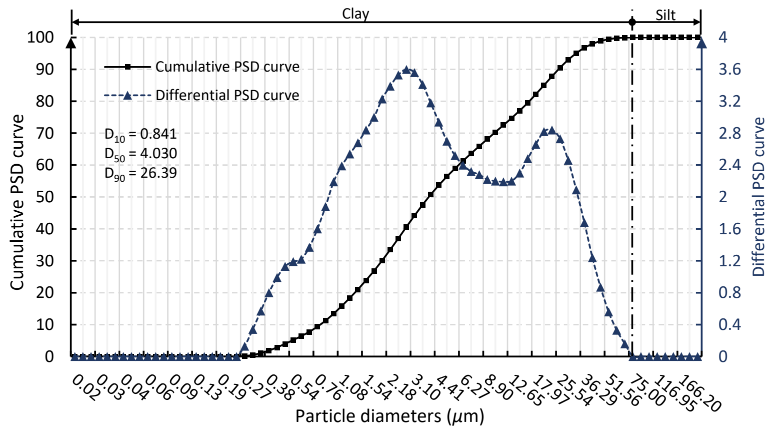

Figure 1: Particle size distribution of the test soil.

The length of the used model box is 90 cm, determining a similarity ratio of 50. Due to the nonlinear nature of soil properties, the similarity relationship between the scaled model and the prototype site is established via the Buckingham law [42, 43]. The mechanical parameter similarity relationship between the scaled model's soil and that of the prototype site, as outlined in Table 1, is employed for reference.

2.2. Layout of sensors

To capture the seismic response of clay soil, a series of sensors are pre-embedded in the slope model. The piezoelectric accelerometers are utilized to record the seismic responses of acceleration which are designed with shear structures that exhibit desirable features, such as low base strain, high immunity to temperature changes, compact size, and consistent performance. Further, to record the seismic response of mechanical properties, four dynamic earth pressure gauges are also pre-embedded in the slope. Additional information about the parameters of the used sensors are listed in Table 2. Note that the dynamic earth pressure gauge is buried vertically, aligned with the bottom surface, and its probe was parallel to the left side boundary of the model box. The specific locations of sensors are illustrated in Figure 2.

Table 1: Similarity relationship of soil mechanical parameters between the scaled model and the prototype site.

Scaling factor λ	Scaling law	Scaling factor λ	Scaling law
Cohesion c	$\lambda_c/(\lambda_l\lambda_g\lambda_\rho)$=1	Acceleration a	$\lambda_a/(\lambda_l\lambda_f^2)$=1
Stress σ	$\lambda_\sigma/(\lambda_l\lambda_g\lambda_\rho)$=1	Elastic modulus E	$\lambda_E/(\lambda_l\lambda_g\lambda_\rho)$=1
Gravitational acceleration g	$\lambda_g/(\lambda_l\lambda_f^2)$=1	Time t	$\lambda_t/(\lambda_l^{0.5}\lambda_g^{-0.5})$=1
Mechanical parameter	**Symbol**	**Dimension (MLT)**	**Scaling factors**
Length	l	[L]	λ_l=50
Density	ρ	$[M][L]^{-3}$	1
Cohesion	c	$[M][L]^{-1}[T]^{-2}$	$\lambda_c=\lambda_l\lambda_g\lambda_\rho$=50
Gravitational acceleration	g	$[L][T]^{-2}$	1
Friction angle	φ	-	1
Elastic modulus	E	$[M][L]^{-1}[T]^{-2}$	$\lambda_E=\lambda_l\lambda_g\lambda_\rho$=50
Strain	ε	-	1
Stress	σ	$[M][L]^{-1}[T]^{-2}$	$\lambda_\sigma=\lambda_l\lambda_g\lambda_\rho$=50
Acceleration	a	$[L][T]^{-2}$	1
Time	t	[T]	$\lambda_t=(\lambda_a/\lambda_l)^{-0.5}$=7.07
Frequency	f	$[T]^{-1}$	$\lambda_f=(\lambda_a/\lambda_l)^{0.5}$=0.14

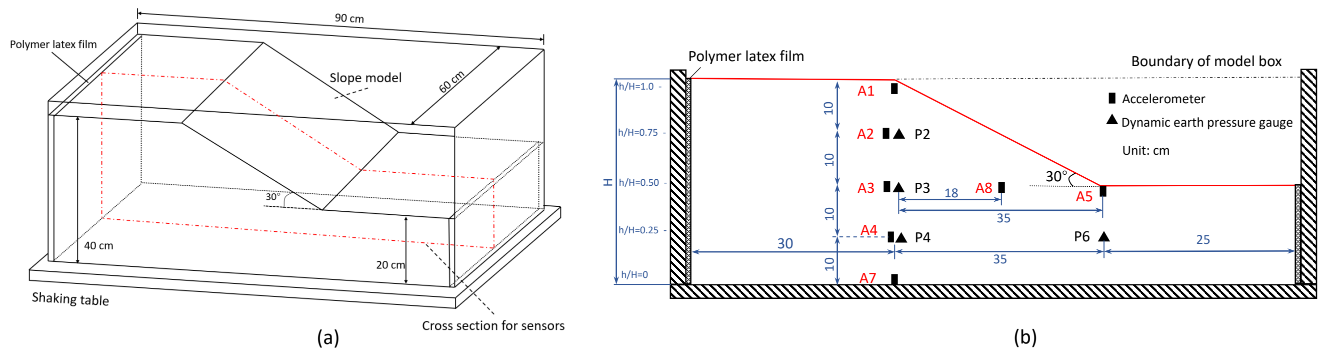

Figure 2: Schematic of geometry and sensor installation for shaking table test. (a) Sketch view of slope model; (b) sensors arrangement.

Table 2: Sensors parameters.

Name	Sensor type	Measuring range	Frequency	Amount
Piezoelectric accelerometer	1A119E	0 - 500 m/s^2	0.5 - 12000 Hz	7
Dynamic earth pressure gauge	CYY9	-50 - +50 kPa	1 - 3000 Hz	4

2.3. Input ground motion

To investigate the seismic responses of the slope, ground motion records in a typical earthquake, namely the Imperial Valley-06 Earthquake, are adopted from the Pacific Earthquake Engineering Research Center (PEER) NGA-West2 databases [44]. The ground motion RSN 158 H1 is included, where 158 accounts for the Recorded Sequence Number (RSN) and 'H1' represents the horizontal 1 in the PEER NGA-West2 Flatfile. Based on the original ground motion, the peak ground acceleration (PGA) of recorded ground motion is amplitude modulated. Overall, six cases are considered, as shown in Table 3. The velocity, acceleration, spectral acceleration, and Fourier spectrum of the selected ground motions are illustrated in Figure 3. It is pointed out that, the mainshock sequence and the aftershock sequence are normally distinct. For the objectives of the present study, which predominantly aims to verify the proposed methodology, a simplified assumption is adopted. Specifically, it is assumed that the aftershock sequence is identical with the mainshock sequence and that the amplitude is adjusted through the PGA. Moreover, in order to reduce as much as possible the experimental error caused by the reflections of the seismic excitation on boundaries, a polymer latex film is placed in the model box during tests.

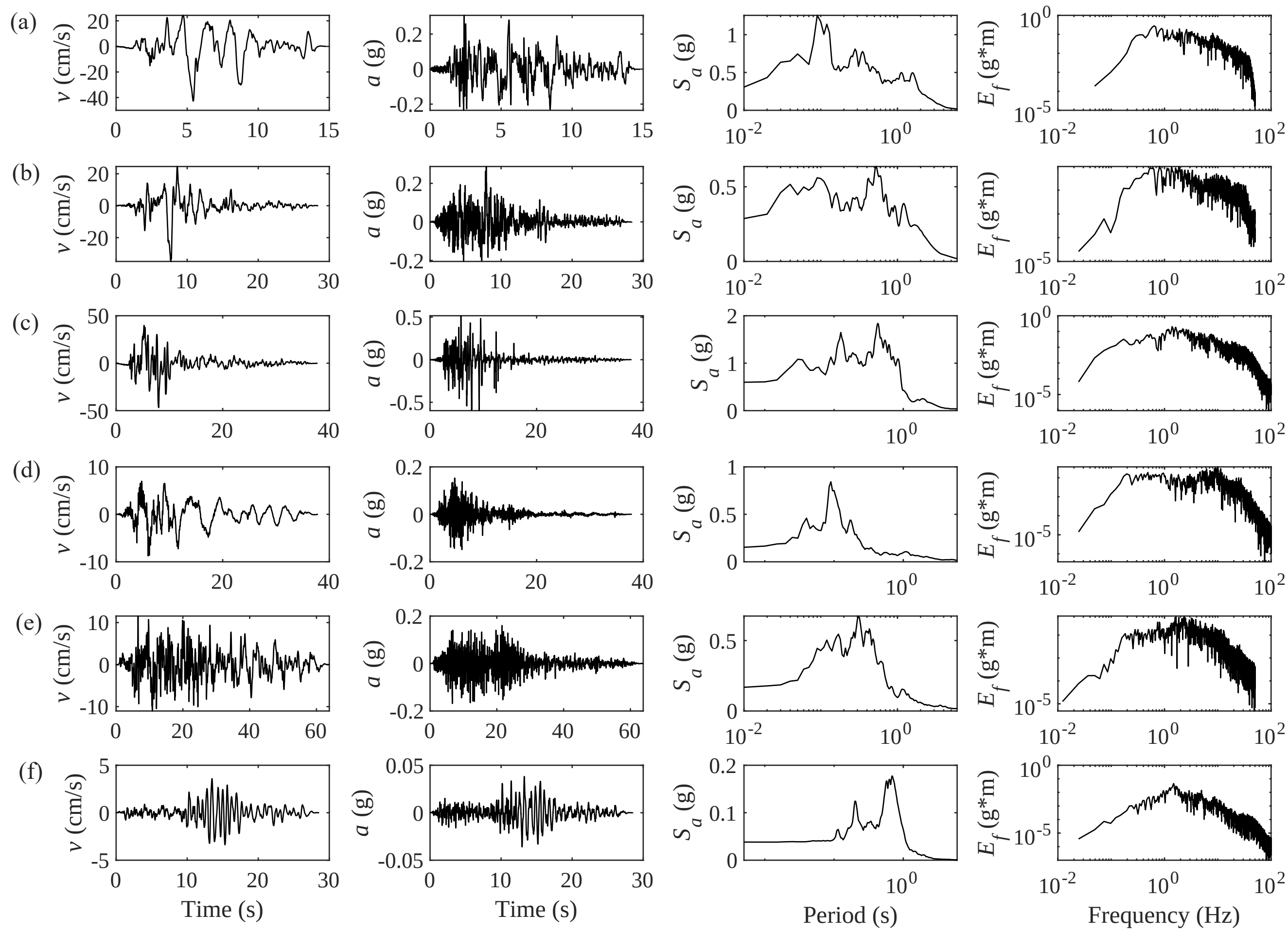

Figure 3: Velocity (v), acceleration (a), 5% damped spectral acceleration (S_a) and Fourier spectrum (E_f) of selected ground motions in shaking table tests. (a) RSN 158 Horizontal 1, (b) RSN 159 Horizontal 1, (c) RSN 160 Horizontal 1, (d) RSN 161 Vertical, (e) RSN 164 Horizontal 1, (f) RSN 166 Vertical in PEER NGA-West2 databases.

Table 3: Designed cases for the shaking table tests.

No.	RSN	Type	Duration (s)	Input peak acceleration (IPA)
Case 1	158H1	PLGM	15	0.36g, 0.30g, 0.22g, 0.18g, 0.08g
Case 2	160H1	PLGM	38	0.30g, 0.27g, 0.22g, 0.15g, 0.07g
Case 3	159H1	PLGM	28	0.30g, 0.21g, 0.18g, 0.14g, 0.09g
Case 4	164H1	NPGM	64	0.37g, 0.27g, 0.22g, 0.16g, 0.07g
Case 5	161V	NPGM	17	0.16g, 0.13g, 0.11g, 0.09g, 0.05g
Case 6	166V	NPGM	29	1.19g, 1.02g, 0.84g, 0.65g, 0.50g, 0.37g, 0.30g, 0.22g, 0.15g

2.4. Procedure of test

The Shake Table II system developed by Canadian Quanser Inc. is used to carry out the shaking table tests and a high-speed camera is positioned on top of the model box to observe the deformation of the entire model. Additional information about the shake table is provided in Table 4, while information about the dynamic data acquisition system, the high-speed camera, the Shake Table II system and the sensors is depicted in Figure 4.

The data acquisition procedure comprised the following steps:

(1) Measurement of the geometric dimensions of the model along the inner wall of the model box.

(2) Placement of the polymer latex film at the designated location within the model box to simulate the flexible boundary.

(3) Introduction of prepared soil samples into the model box, followed by compaction. To ensure the optimal degree of compaction, each layer is compacted to a controlled thickness of 5 cm.

(4) Installation of sensors at selected positions during the construction of the model.

(5) Verification to ensure the precision of the sensor signals. This is conducted upon completion of the model assembly, and involved connecting the sensors to the dynamic data acquisition system.

(6) Application of seismic load under various operating conditions and collection of data from each sensor channel.

Table 4: Shaking table parameters.

Parameter	Value	Unit	Parameter	Value	Unit
Length	61	cm	Width	46	cm
Height	13	cm	Area of payload	46 × 46	cm^2
Maximum payload	15	kg	Maximum stroke of table	7.5	cm
Working frequency range	0 - 20	Hz	Maximum full load acceleration	2.5	g

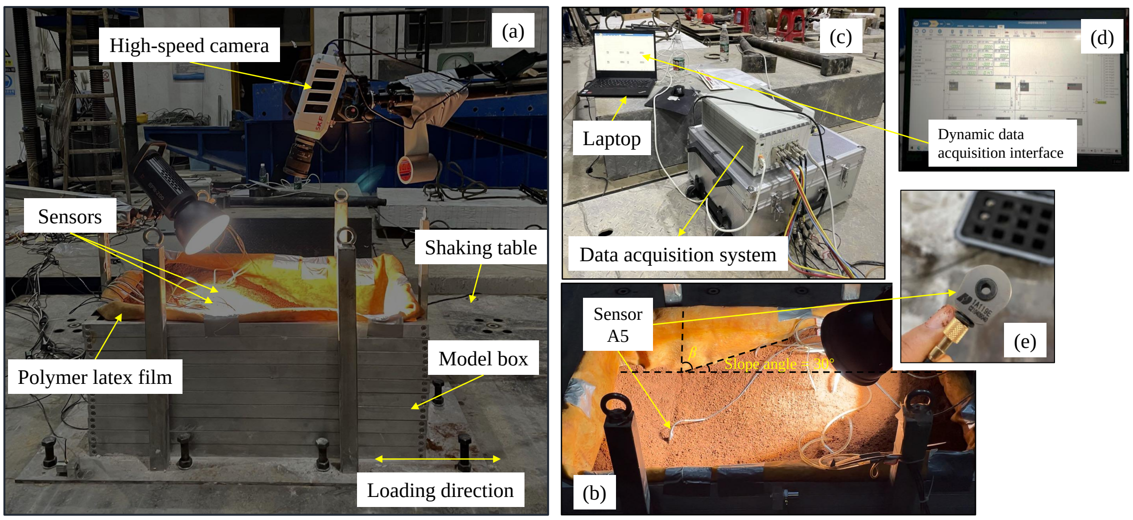

Figure 4: Shaking table test system. (a) Overall model status; (b) model dimension; (c) dynamic data acquisition system; (d) acquisition interface; (e) sensor.

3. Model updating approach for slope seismic analysis

3.1. Random field discretization with dimensionality reduction method

In model updating, the initial step involves establishing the prior distribution. We consider a prior distribution as a random field represented with the K-L expansion. Herein, we employ the squared exponential autocorrelation function $\rho(x, y)$ to describe the autocorrelations between points as

$$\rho(x,y) = exp\left\{-\pi(\frac{\Delta x}{\Theta_x})^2 - \pi(\frac{\Delta y}{\Theta_y})^2\right\} \tag{1}$$

where Θ_x, and Θ_y are the scale of fluctuation (SOF) along x-, and y-axis; Δx, and Δy denote the difference in absolute distance between two points along x-, and y-axis. The most commonly used methods for the problem of random fields generation include, indicatively, the covariance matrix decomposition method [45], the spectral decomposition method [46], the Karhunen-Loève (K-L) expansion method [47], optimal linear estimation method [48], and the modified linear estimation method [49]. Herein, the K-L expansion method is adopted to generate the random field. The two-dimensional Gaussian random field generated using the K-L expansion can be expressed as

$$U(x, y; \theta) = \mu(x, y) + \sigma(x, y) \sum_{i=1}^{\infty} \sqrt{\lambda_i} \varphi_i(x, y) \theta_i \tag{2}$$

where U represents the variable; $\mu(x, y)$ and $\sigma(x, y)$ denote the mean and standard deviation of the random field, respectively. Further, θ_i is the i-th independent and unrelated normal random variable, and λ_i and $\varphi_i(x, y)$ are the i-th eigenvalue and corresponding eigenvector of $\rho(x, y)$, respectively. The eigenvalues and eigenfunctions are derived as the solutions to the Fredholm second-kind integral equations

$$\int_D \rho(x_1, y_1; x_2, y_2) \varphi_i(x_1, y_1) dx_1 dy_1 = \lambda_i \varphi_i(x_2, y_2) \tag{3}$$

where D denotes the discrete region; (x_1, y_1) and (x_2, y_2) denote the coordinates of any two points within the two-dimensional computational domain. Compared to other discretization methods for random fields, the advantage of the K-L expansion method lies in its ability to achieve relatively high computational accuracy with fewer random variables, avoiding in such way the need to derive the complete set of eigenvalues. Besides, the dimensionality reduction of the K-L expansion method can be utilized to convert the target of inverse analysis from complex high-dimensional spatial variables to simpler low-dimensional normal random variables, thus enabling Bayesian probabilistic inverse analysis. Hence, we adopt a dimensionality reduction of the K-L expansion and utilize its truncated form to generate the random field in the form

$$U(x, y; \theta) = \mu(x, y) + \sigma(x, y) \sum_{i=1}^{n} \sqrt{\lambda_i} \varphi_i(x, y) \theta_i \tag{4}$$

where n denotes the truncation order. In general, the n should be sufficient to retain at least 95% of the total variance of the actual variability compared to the overall variability; that is

$$\frac{\sum_{i=1}^{n} \lambda_i}{\sum_{i=1}^{\infty} \lambda_i} = 0.95 \tag{5}$$

and the process diagram for the dimensionality reduction of the K-L expansion is illustrated in Figure 5.

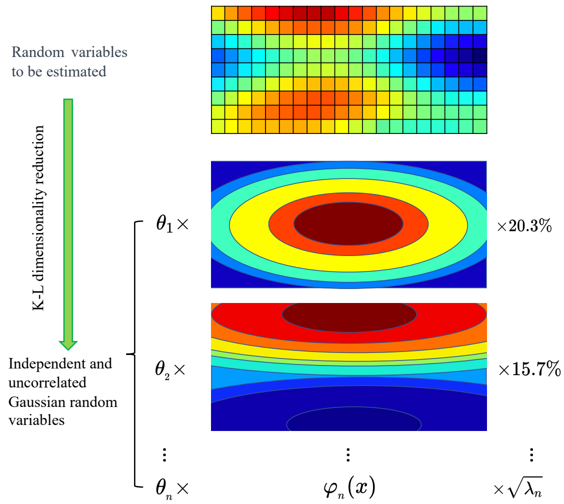

Figure 5: The process scheme for dimensionality reduction of K-L expansion method.

3.2. Bayesian model updating algorithm

The adaptive Bayesian updating with structural reliability methods - subset simulation (aBUS-SuS) method is capable of effectively analyzing high-dimensional rare failure problems, leading to increasing the speed of approximation in the failure domain of the sample space. Herein, we will provide a detailed introduction to the Bayesian updating with structural reliability methods (BUS) algorithm coupled with subset simulation (SuS) for addressing Bayesian inverse problems. The impact of site-specific data on uncertainty parameter distribution can be assessed through the evaluation of the posterior probability density function (PDF) denoted as $f''_X(x)$ for the random variable X. Utilizing Bayes' theorem, the estimation of $f''_X(x)$ is

$$f''_X(x) = aL(x)f'_X(x) \tag{6}$$

where a represents a normalization constant; $f'_X(x)$ is the prior PDF; $L(x)$ denotes the likelihood function; The detailed definition of the likelihood function will be provided in Section 4.1. $L(x)$ is proportional to the probability of the event; X equals the site-specific information for x; that is

$$L(x) \propto P(Z \mid X = x) \tag{7}$$

where Z represents observation event and $P(\cdot)$ represents the probability of event. Specifically, the BUS first defines an equivalent failure (Ω_Z) as

$$\Omega_Z = \{w - cL(x) < 0\} \tag{8}$$

where w is the simulation value of a random variable W, uniformly distributed in the interval $[0, 1]$; c is the likelihood multiplier. In SuS, the probability $P(Z)$ is expressed as the product of larger conditional probabilities associated with a series of nested intermediate events, allowing for estimation as

$$P(Z) = P[w - cL(x) < 0] = P(Z_1)\prod_{i=2}^{m} P(Z_i \mid Z_{i-1}) \tag{9}$$

where m represents the count of subset levels necessary to reach the failure domain, with each subset level comprising N_l samples; $Z_1 \supset Z_2 \supset ... \supset Z_m$ represent intermediate events denoted by $Z_i = \{w - cL(x) < g_i\}$, where g_i signifies the thresholds with the condition $g_1 > g_2 > ...g_{m-1} > 0 \geq g_m$; $P(Z_i \mid Z_{i-1})$ is conditional probability of Z_i given Z_{i-1}; the g_i values can be selected to achieve a target value, p_0, for the intermediate conditional probability.

To determine the initial threshold, g_1, Monte Carlo sampling is employed on samples conditioned on a specific event. Subsequently, for estimating subsequent thresholds, $g_i(i = 2, \ldots, m)$, MCMC sampling is utilized on samples conditioned on intermediate events. In this context, the component-wise Metropolis–Hastings algorithm is utilized to obtain samples within intermediate domains. That has been demonstrated to be effective in sampling from high-dimensional conditional distributions [50].To ensure computational precision and efficiency in subset simulation computations, it is crucial to first determine the appropriate value of c. Nevertheless, in most cases, it is not straightforward to find an analytical solution for the maximum likelihood function, which complicates its determination. In the present study, an adaptive approach is employed to automatically deduce the value of c, and more details can be found in Betz et al. [51], that is

$$-\mathrm{ln}c_i = \max[-\mathrm{ln}c_{i-1}, \{\ln(L(x_{i,k}))\}] \tag{10}$$

where $i = 1, 2, ..., m$ and $k = 1, 2, ..., N_l$; c_{i-1} is the likelihood multiplier in the i-th subset level. Additionally, combining with Eq. 2, it is easy to transform the issue from the origin random variable X to the variable $U = [U_1, ..., U_n]$:

$$X = \mathrm{T}(U_1, ..., U_n) \tag{11}$$

where T denotes classic transformations, e.g., marginal transformation in Nataf model. The implementation of the proposed method is provided for completeness. A brief description is also shown in Figure 6.

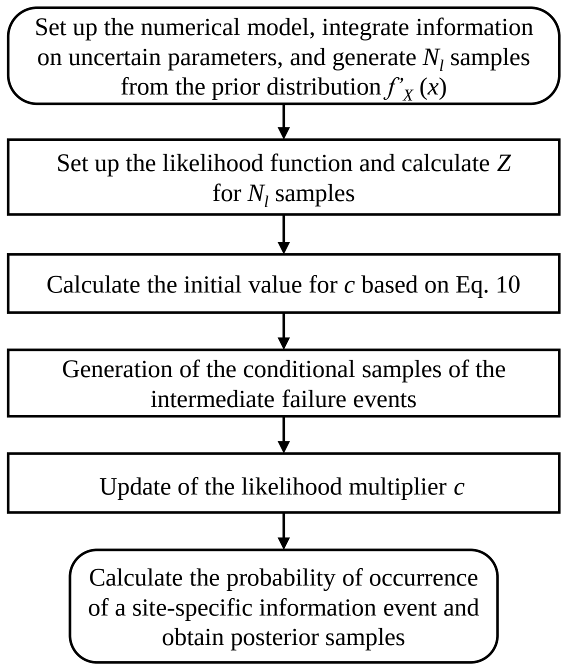

Figure 6: Flow chart of the proposed approach.

4. Numerical implementation of model updating approach

4.1. Prior knowledge and likelihood function

In the present study, the slope response data obtained during shaking table tests are used as site information. For instance, consider the peak acceleration value a_{p}. Then, the relationship between the i-th set of measured values $a_{\mathrm{p},i}$ and the corresponding calculated values $a_{\mathrm{p}}(q_i)$ at position q_i can be expressed as

$$a_{\mathrm{p},i} = a_{\mathrm{p}}(q_i) + \varepsilon_i, i = 1, 2, ..., n_d \tag{12}$$

where ε_i denotes measurement error. Taking into account the correlation among measurement errors in two sets of arbitrary experimental data, the likelihood function associated with n sets of experimental data is formulated as

$$L(x) = k \exp\left\{-\frac{1}{2}[\boldsymbol{a}_\mathrm{p} - a_\mathrm{p}(\boldsymbol{q})]^\mathrm{T}\boldsymbol{\Sigma}^{-1}[\boldsymbol{a}_\mathrm{p} - a_\mathrm{p}(\boldsymbol{q})]\right\} \tag{13}$$

where $k = [(2\pi)^{-\frac{n_d}{2}}|\Sigma|^{\frac{1}{2}}]^{-1}$; $\boldsymbol{a}_\mathrm{p} = [a_{\mathrm{p},1}, a_{\mathrm{p},2}, ..., a_{\mathrm{p},n}]^\mathrm{T}$ is the experimental data sample vector; $\boldsymbol{q} = [q_1, q_2, ..., q_{n_d}]^\mathrm{T}$ represents the position vector of experimental points. Further, $\boldsymbol{\Sigma}^{-1}$ represents the inverse matrix of the autocovariance matrix $\boldsymbol{\Sigma}$, composed of the variance σ^2 of the measurement errors recorded by each monitoring instrument and the correlation coefficient between the measurement errors.

4.2. Random field construction

The non-linear dynamic behavior of soil follows the hyperbolic-hysteretic model as illustrated in Figure 7. The hyperbolic-hysteretic model has been verified for its effectiveness on kaolin and clays based on a series of centrifuge tests conducted by Banerjee et al. [52] and Liu and Zhang [53]. Chen et al. [54] have also verified the seismic response of soil-buried tunnels on the basis of hyperbolic-hysteretic model. The maximum (or small-strain) shear modulus G_max of hyperbolic-hysteretic model is given by

$$G_\mathrm{max} = A \times (p^{'})^n \tag{14}$$

where $p^{'}$ represents the mean effective normal stress, and A and n denote calibration parameters. The wide applicability of Eq. 14 has been demonstrated by its adoption in numerous studies (e.g. [52, 55]). Following Liu and Zhang [53], the spatial variability of G_max has a significant effect on soil seismic response, and neglecting this effect leads to an inaccurate assessment of the risk of slope failure. According to previous studies [56], the value of n is typically considered fixed, with a common choice being 0.653. However, the value of A often exhibits a significant range of variation. Notably, a variation of one order of magnitude is observed in certain soils. Therefore, the spatial variability of G_max is reflected in the A value. The mean value of A was set to 2060, in line with the work conducted by Liu and Zhang [53]. A coefficient of variation (COV) of 0.2 is adopted for A in agreement with the COV values reported by Schevenels et al. [57] and Ayad et al. [58], who also modeled G_max as a random field. It is important to note that the mean effective normal stress p' in Eq. 14 varies with depth, typically increasing, which leads to additional variability in $G_{\max}$. Consequently, the overall variability of $G_{\max}$ surpasses that of A depending on the depth range under consideration. When dealing with in-situ test data, it is crucial to acknowledge the potential amplification of variance due to measurement errors, as discussed in Phoon and Kulhawy [59]. The present study has not separately accounted for measurement errors. In summary, to reduce the uncertainties brought by the spatial variability of $G_{\max}$, the $G_{\max}$ random field is incorporated into the proposed model updating approach. On basis of prior knowledge regarding $G_{\max}$, the random field is simulated, with typical realization presented in Figure 8, where darker zones indicate larger $G_{\max}$ values.

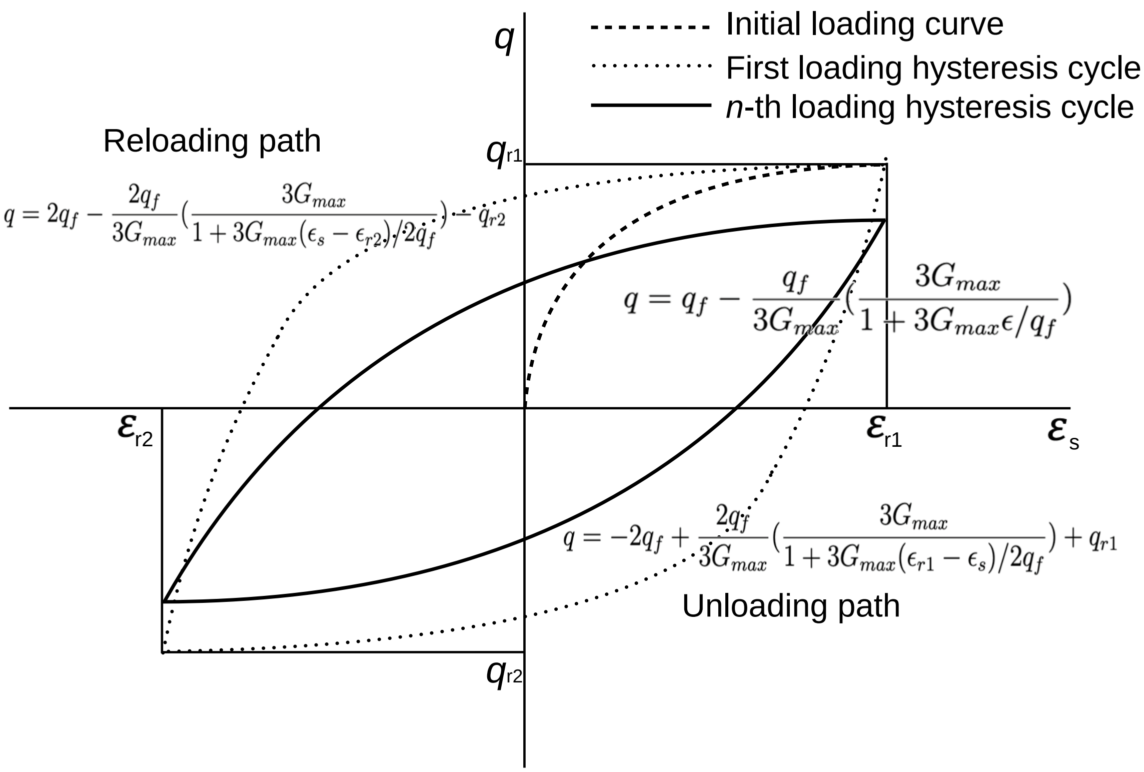

Figure 7: Clay soil dynamic constitutive model.

4.3. Model description

In this section, the potential of the herein proposed model updating approach is demonstrated by considering the problem of the seismic response evaluation of a slope dynamic system. To this end, a finite element model is established using the commercial finite element software ABAQUS version 6.14. The mesh scale and the details of the boundary conditions are depicted in Figure 8. The model has seven accelerometers installed as sensors, while it contains 5453 elements with

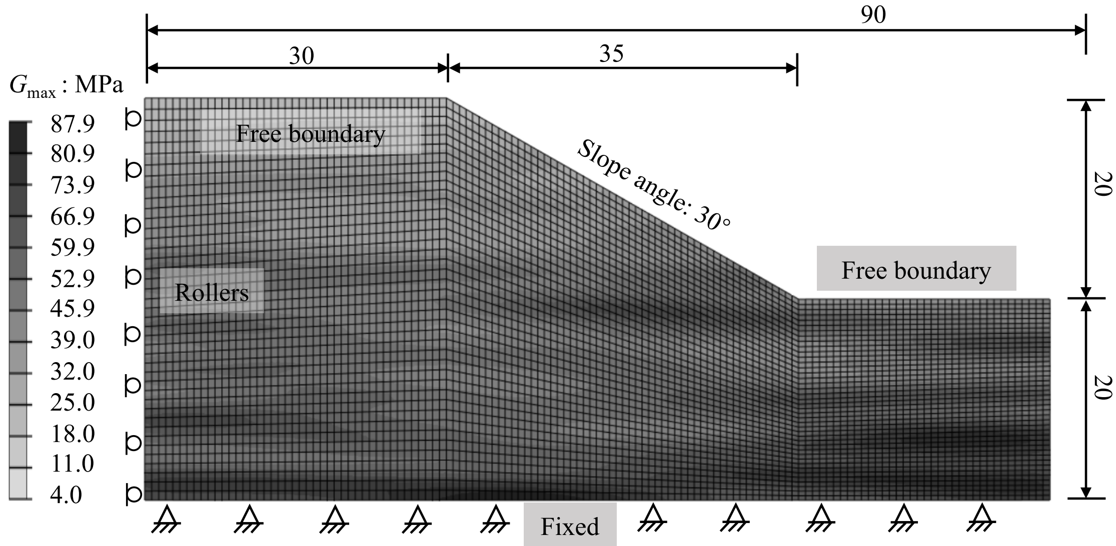

Figure 8: A typical realization for $G_{\max}$ random field.

types of four-node plane strain element (CPE4R). To mitigate the discretization errors arising from random field discrete processes, the mesh scale is configured at 4.2% of the correlation length for effective control [60]. The analysis comprises the following two steps. First, an initial stress equilibrium is achieved, and then, a nonlinear time history analysis of the ground motion is conducted. Based on the mechanical parameters of the red clay used in the experiment, the numerical simulation parameters are configured as listed in Table 5. The left and right boundaries are characterized by free-roller boundary conditions, whereas the bottom exhibits complete fixity. The input ground motion is applied in the horizontal direction. To maintain consistency with the shaking table experiment, the same input ground motion selected from the PEER NGA-West2 database, as well as the acceleration time history, and the frequency spectrum were employed. These are depicted in Figure 3.

5. Results and discussions

As mentioned in Section 2, it is imperative to examine the dynamic characteristics of slopes, focusing on the acceleration evolution, the slope dynamic stability, and the amplification effects across various slope regions. The findings presented in this section are derived from the analysis of 34 seismic response cases.

Table 5: Soil mechanical parameters and modeling information.

Mechanical parameter	Symbol	Unit	Value
a. Deterministic parameters			
Density	ρ	g/cm^3	1.6
Poisson's ratio	μ	-	0.3
Dilation angle	ψ	$^\circ$	0
Friction angle	φ	$^\circ$	25
Effective gravity	γ	kN/m^3	6
Coefficient of earth pressure at rest	K_0	-	0.5774
Slope height	H	m	20
Slope angle	α	$^\circ$	30
b. Statistical properties of random field for $G_{\max}$ of inhomogeneous soils			
Mean average of A	-	-	2060
Coefficient of variation	COV_A	-	0.2
Horizontal correlation length	Θ_H	m	16
Vertical correlation length	Θ_V	m	1.5

5.1. Experimental characteristics for the slope dynamic system

5.1.1. Seismic evolution of acceleration

In this section, the acceleration response is analyzed by examining different accelerometers positioned at various locations in the model. Specifically, accelerometers positioned at surface (A1), top (A2), middle (A3), and bottom (A4) are considered to investigate the patterns and trends in the acceleration response. The response peak acceleration (RPA) for each of these cases is illustrated in Figure 9. The results indicate that, as the loading intensity increases, the peak acceleration at different locations also increases correspondingly. Further, it is evident from Figure 9 that, for a given loading intensity, the type of input seismic excitation significantly influences the RPA values. Specifically, the RPA induced by PLGM is greater than, or at least equal to the corresponding value of the NPGM. For instance, the RPA values for cases subjected to PLGMs and NPGMs with the loading intensity of $0.30g$ and $0.22g$, respectively, at different elevations (i.e. h = 40 cm, h = 30 cm, and h = 20 cm) are selected and their RPA values are listed in Table 6. In Table 6, Nos. 1 - 3 are the RPA obtained from cases subjected to PLGMs, and they are all greater than those subjected to NPGMs (No. 4). Also, the RPA values of Nos. 5 and 6 are greater than these of Nos. 7 and 8. The phenomenon is enhanced in the experimental cases with higher loading intensities. Specifically, with an increase in height (e.g. h/H = 1.0), there is a more significant growth in the acceleration values, and when the loading intensity exceeds $0.2g$, this growth becomes substantially amplified. In other words, a site amplification effect is observed in the acceleration values. This observation highlights that the shear modulus of the soil varies at different depths. The acceleration response of slope dynamic system subjected to RSN 158H1 with a loading intensity of $0.22g$ is shown as a representative example in Figure 10. When comparing A1 (h/H=1.0), A5 (h/H=0.5), and A7(h/H=0), it becomes evident that an increased elevation leads to an acceleration amplification at every time point. Furthermore, despite the similarity of the Fourier spectra in Figure 10, there is a consistent amplification across all frequency domains.

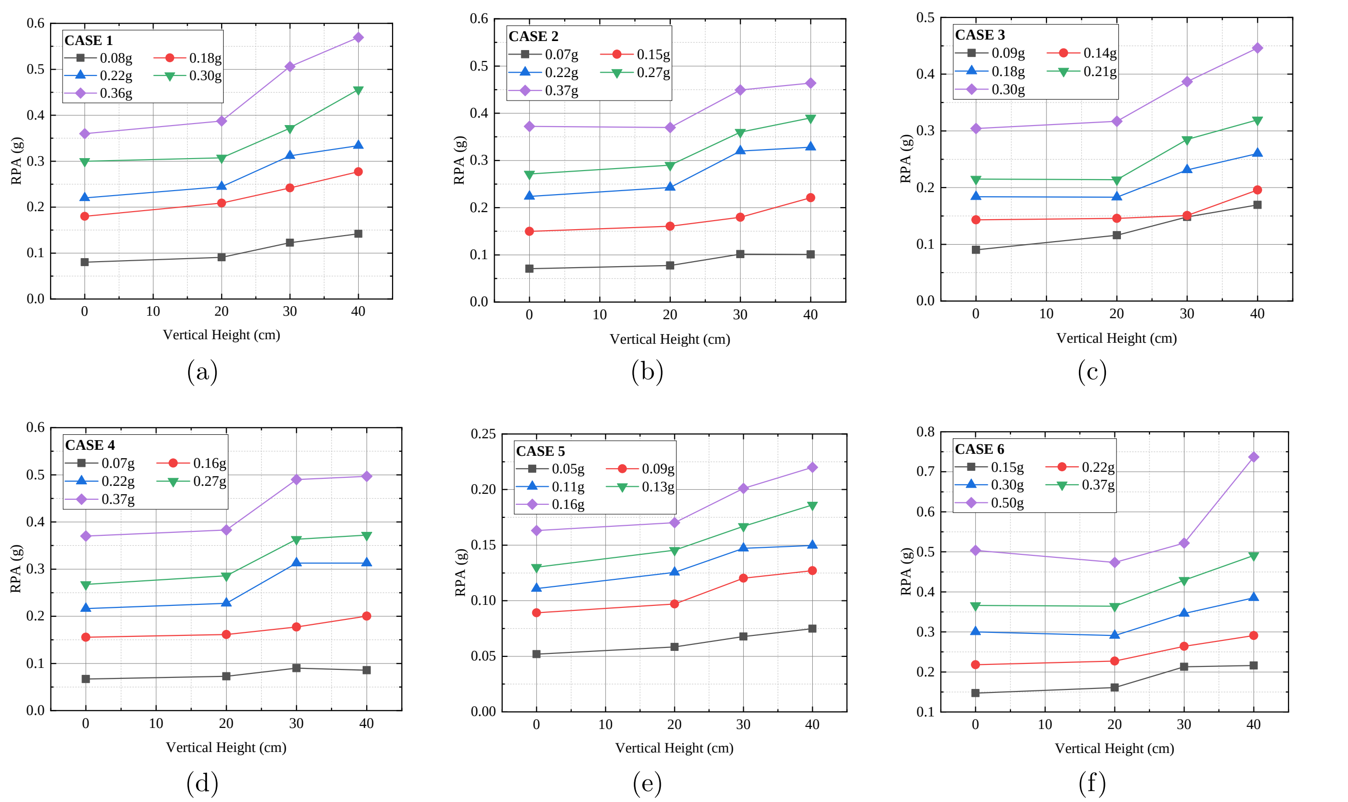

Figure 9: Relationship between the RPA and the vertical elevations of the slope model.

In the ensuing analysis, the seismic amplification effect is evaluated by introducing the acceleration-amplification factor, which is defined as

$$F_{\mathrm{aa}} = \frac{P_{\mathrm{r}}}{P_{\mathrm{input}}} \tag{15}$$

where P_{r} and P_{input} are the peak value of the recorded signal and the peak value of input seismic excitation, respectively. The variation of the F_{aa} with respect to different values of the vertical elevation is shown in Figure 11. Clearly, as the vertical elevation of the sensor position increases, the F_{aa} value also increases. During the testing process for all cases, the acceleration amplification

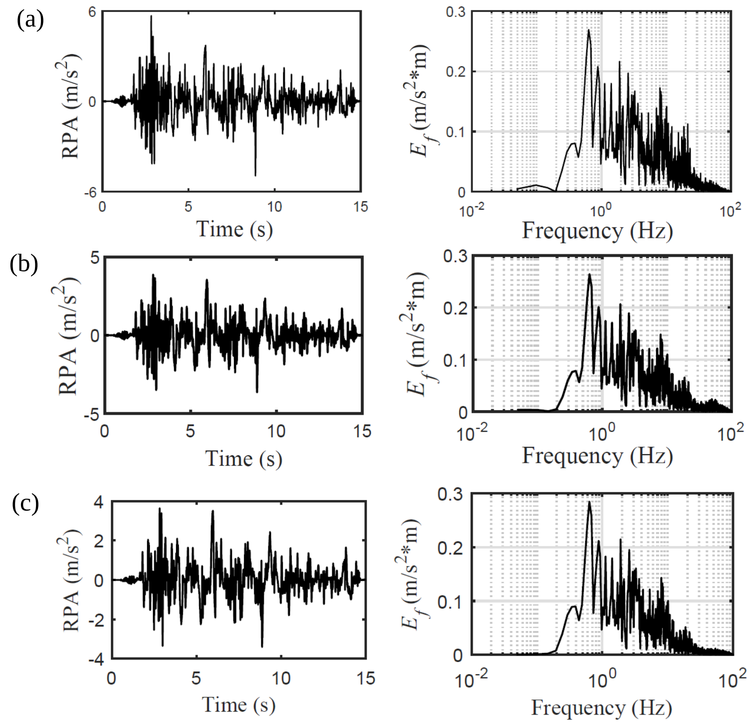

Figure 10: Dynamic response of acceleration and Fourier spectrum under RSN 158H1 with 0.36g loading intensity at (a) A1; (b) A5; (c) A7.

effect is observed. This phenomenon is consistent with the observation by Chen et al. [61], which proves the effectiveness and reliability of the herein reported experimental results. Furthermore, Figure 11 illustrates a significant increase in the F_{aa} at h/H=1.0 under PLGMs, as compared to h/H=0.75. At h/H=1.0, under the same loading intensity (e.g. 0.30g), the F_{aa} values for Case 3 are slightly larger than those for Case 6, indicating that PLGMs may have a more destructive impact on the topsoil layer. The variation trends of the F_{aa} for the cases subjected to PLGMs (Cases 1 - 3) is more regular and similar as compared to the cases when the F_{aa} is subjected to NPGMs (Cases 4 - 6). Notably, the maximum observed F_{aa} value occurs specifically under a PLGM in Case 3, with a value of 1.88. During the transition from h/H=0.75 to h/H=0.5, PLGMs exhibit a steeper slope compared to NPGMs, indicating a more severe impact. In addition, due to the characteristics of PLGM, the peak ground displacement (PGD) for NPGM (recorded sequence RSN 166V, Case 6) is 2.85 cm under IPA equal to 0.30g. However, the PGD for PLGM (e.g. recorded sequence RSN 158H1, Case 1) with the same IPA magnitude (i.e., 0.30g) is 6.87 cm, which is 2.41 times larger than the PGD of NPGM. That is, PLGMs possess higher and more concentrated energy. This explains why PLGM can induce a more destructive impact despite its shorter duration (i.e. the duration of the selected PLGM RSN 158H1 is 15 s, while that of NPGM

RSN 166V is 29 s), emphasizing its adverse effects on the slope structure.

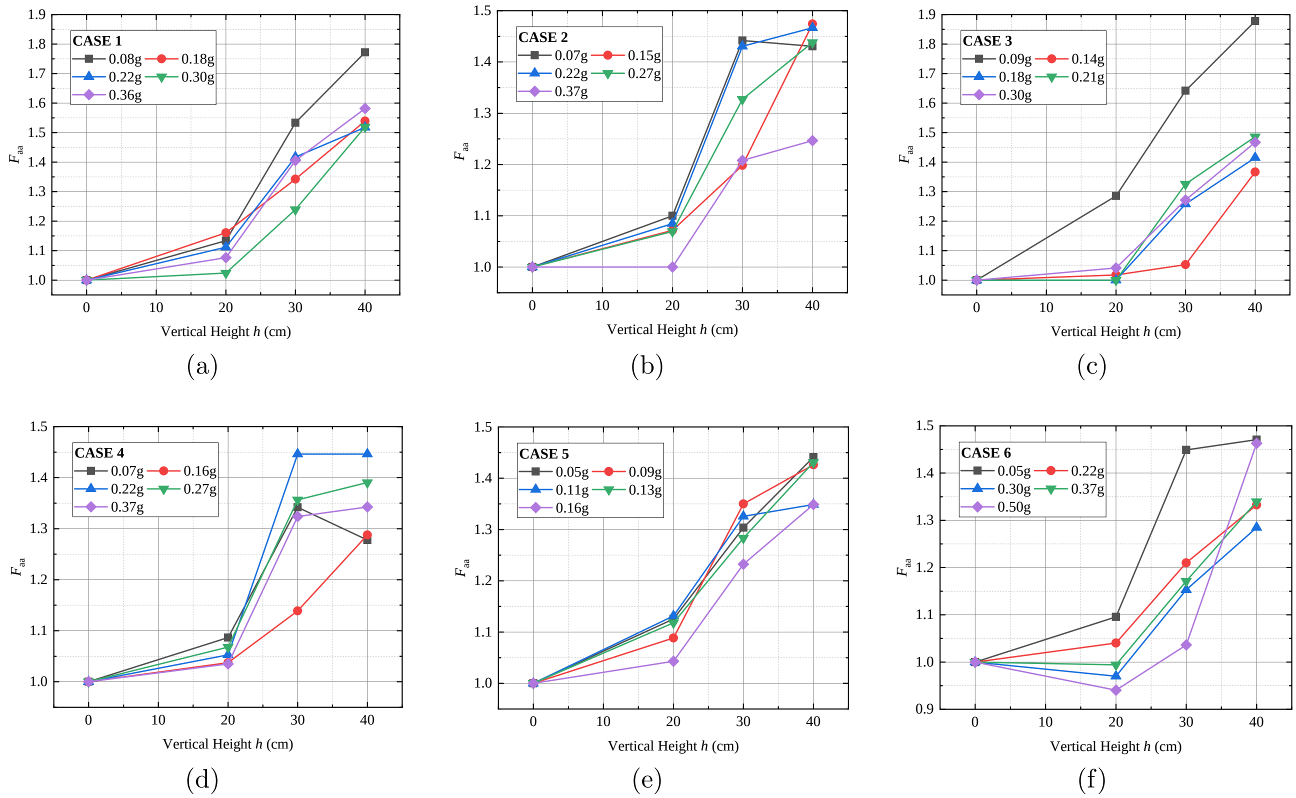

Figure 11: Relationship between acceleration-amplification factor (F_{aa}) and the vertical elevations (h).

Table 6: RPA at different elevations (h).

No.	Case	Type	Loading intensity	h =40 cm	h =30 cm	h =20 cm
1	Case 1	PLGM	0.30g	0.46g	0.37g	0.31g
2	Case 2	PLGM	0.30g	0.46g	0.45g	0.37g
3	Case 3	PLGM	0.30g	0.45g	0.39g	0.32g
4	Case 6	NPGM	0.30g	0.39g	0.35g	0.29g
5	Case 1	PLGM	0.22g	0.33g	0.31g	0.24g
6	Case 2	PLGM	0.22g	0.33g	0.32g	0.24g
7	Case 4	NPGM	0.22g	0.31g	0.30g	0.23g
8	Case 6	NPGM	0.22g	0.29g	0.26g	0.23g

5.1.2. Stability of the slope dynamic system

Figure 12 shows the peak pressure responses at different locations under various loading intensities. The pressure responses demonstrate a nonlinear relationship, as the soil pressures along the same vertical line do not increase linearly with depth, and no significant site amplification effects are observed. Notably, the maximum peak value of 388 Pa is recorded at P3 for Case 3 under a loading intensity of $0.18g$. This high value can be attributed to the horizontal burial of P3 at the foot of the slope, where increased pressure occurs when the slope experiences cracking or tends to slide during the test. To describe the level of dispersion of data distribution for soil pressure response, the concept of interquartile range (IQR) is introduced and defined as:

$$\mathrm{IQR} = Q_3 - Q_1 \tag{16}$$

where Q_3 denotes the value at the seventy-fifth percentile when the data is sorted in ascending order; Q_1 represents the first quartile of the dataset. A larger IQR value indicates greater dispersion of data, implying a wider range of numerical distribution that contains more outliers and extreme values. Conversely, a smaller IQR value suggests lower dispersion of data, with a narrower range of numerical distribution that contains fewer outliers and extreme values.

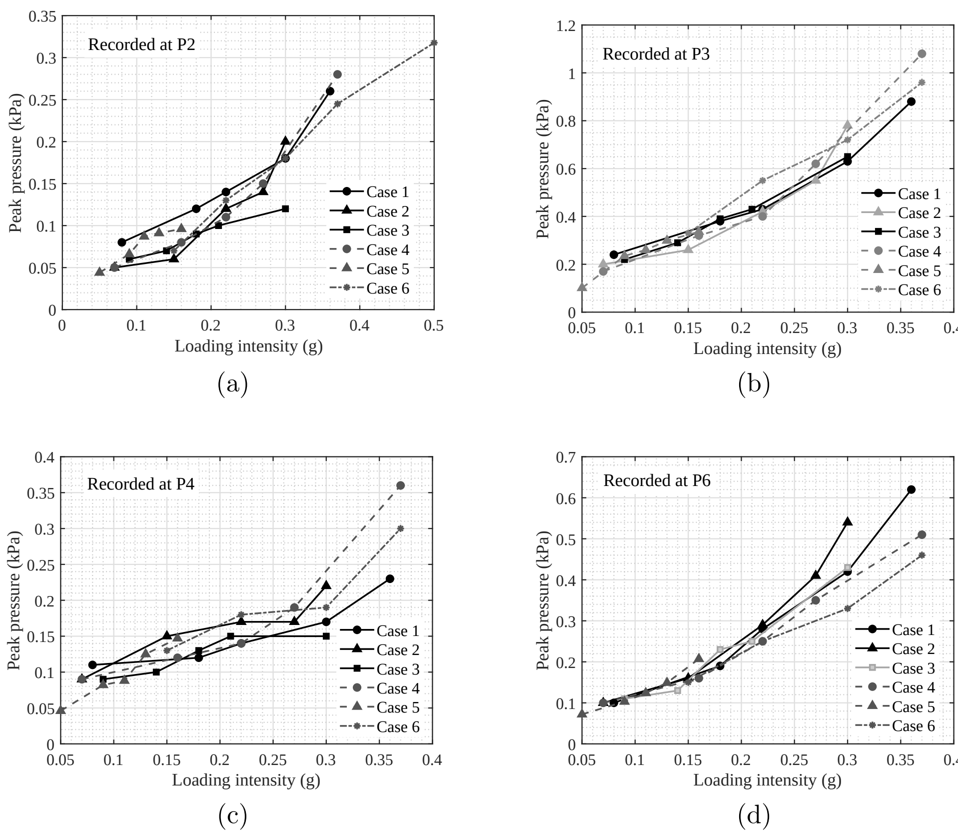

Figure 12: Peak pressure responses for cases under various loading intensities at (a) P2, (b) P3, (c) P4, (d) P6.

As illustrated in Figure 13, the IQR value of Case 3, subjected to a PLGM (IPA $= 0.3g$) at h/H=0.5, is 0.126 kPa, while for Case 6, subjected to a NPGM, the IQR value is 0.055 kPa. This means that the IQR value of PLGM is roughly 2.30 times greater than that of NPGM. It can be observed that the soil pressure response to PLGMs has more data points within a larger interval compared to the pressure responses of NPGMs. The mean value of soil pressure under a NPGM is closer to zero than under a PLGM, as illustrated in Figures 13(b) and (c). Note, in passing, that the mean values at P2 and P6, which are very close to zero, are not marked in the figure. In other words, PLGMs tend to generate pressure distributions with larger peak values, while NPGMs exhibit more concentrated pressure distributions with values oscillating near 0 kPa. Therefore, considering the response of soil pressure and acceleration, it can be concluded that PLGMs are more likely to carry higher and more concentrated energy. That is, compared to NPGMs, PLGMs have a more severe detrimental impact on soil structures.

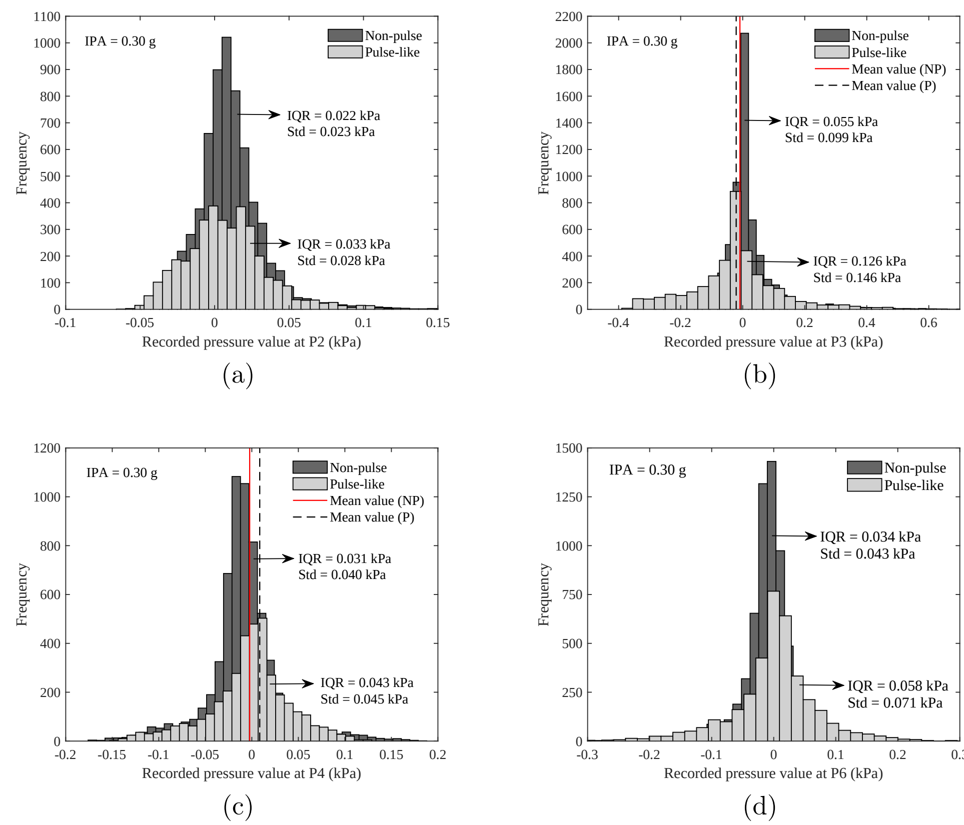

Figure 13: Distribution of pressure values under a 0.30g loading intensity of NPGMs and PLGMs at (a) P2; (b) P3; (c) P4; (d) P6.

5.1.3. Damage and residual deformation

In this section, the damage and residual deformation of clay slopes in the context of seismic response are examined. Case 6 is undertaken subjected to an NPGM (recorded sequence RSN

166V) in order to discern the damage pattern of the clay slope. Moreover, Case 6 incorporates loading intensities of 1.19g, 1.02g, 0.84g, 0.65g, 0.50g, 0.37g, 0.30g, 0.22g, and 0.15g. Herein, a high-speed camera is employed to capture real-time images of the slope shoulder under varying loading intensities. The specific area of capture is illustrated in Figures 14(a) and (b). The ultimate overall crack is developed on the surface of the slope shoulder. The dynamic system fails and dynamic stress ultimately exceeding soil strength, with an overall crack length of 50 cm and a depth of 120 mm (see Figure 14(c)). The specific process is as follows: at the loading intensity of 1.19g, a fine crack emerges on the top surface of slope as illustrated in Figure 14(d). As the loading process progressed, the crack is gradually connected at 1.02g, and a crack is formed from the middle to both ends of the slope at the top free surface as summarized in Figure 14(e). The specific locations of cracks are found at the intersection of the horizontal crest and the inclined free surface of the slope. More specifically, when the loading intensity is 0.84g, the width and length of cracks were thickened, as compared with the cracks obtained under 1.19g and 1.02g loading intensity (see Figure 14(f)). It has been observed that the interaction between tensile and shear forces during loading leads to performance degradation of dynamic systems, making this location a critical failure surface.

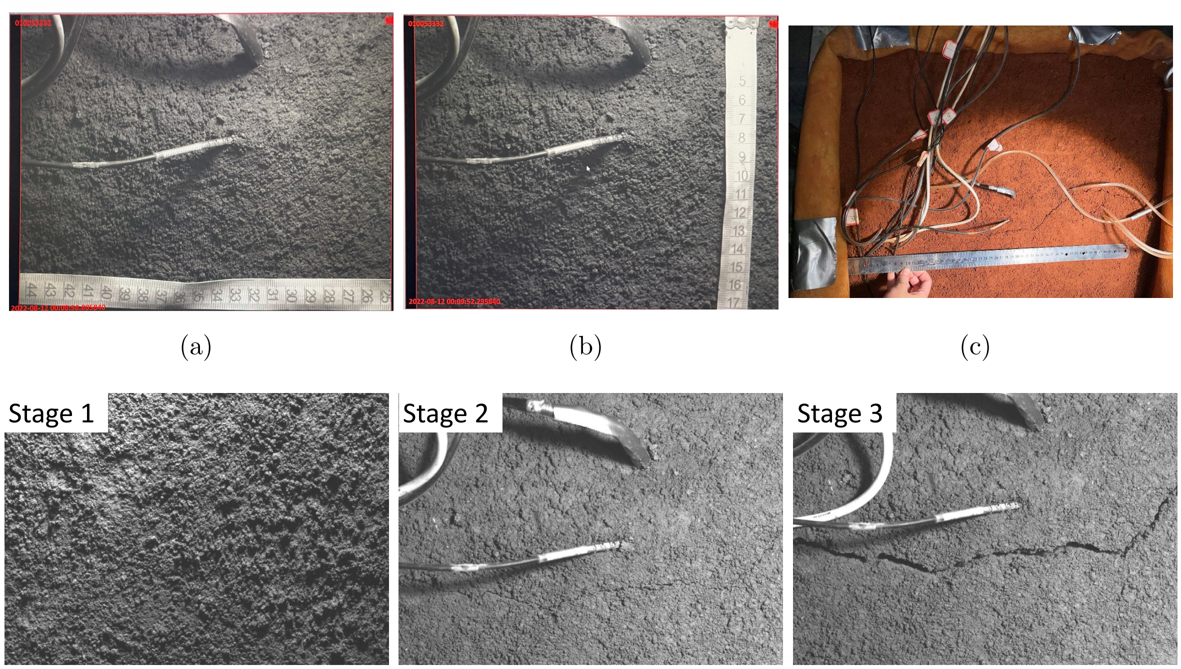

(a) (b) (c)

(d) (e) (f)

Figure 14: The process of fracture expansion as the increase of loading intensity. (a) Length of the specific area of high-speed camera capture; (b) width of the specific area of high-speed camera capture; (c) overall morphology of crack propagation; (d) stage 1; (e) stage 2; (f) stage 3.

5.2. Numerical results

As discussed in Section 4, the data acquired from the shaking table test subjected to ground motion RSN 158H1 from PEER NGA-West2 database are employed, to demonstrate the capability of the proposed computational approach in predicting the seismic response of slope and inverse analysis of the maximum shear modulus distribution in slope dynamic system. Additional detailed information regarding the ground motion RSN 158H1 is illustrated in Figure 3 (a). Typically, the mainshock sequence and aftershock sequence are different. However, for the present study, which primarily aims to validate the proposed methodology, a simplified assumption is employed. The assumption involves using the aftershock sequence kept the same as mainshock sequence but controlling the amplitude through PGA to align with the shaking table tests. Besides, before entering each simulation, it is assumed that the slopes have reached a state of consolidation stability under the influence of self-weight stresses in the soil, without considering changes in the in-situ stress and soil properties. Therefore, the initial stress equilibrium is established first, followed by the application of seismic loads. The specific implementation process is illustrated in Figure 15. Specifically, the loading condition of $0.18g$, denoted as IPA $= 0.18g$, is referred to as the calibration period. During this period, the distribution of the maximum shear modulus is updated based on the collected acceleration response values. At this period, the RPA data gathered at positions A1, A2, A3, and A4 are $0.28g$, $0.24g$, $0.21g$, and $0.18g$, respectively. Subsequently, the period with aftershocks at $0.08g$ (IPA $= 0.08g$) is designated as the validation period, during which the updated distribution of the maximum shear modulus is used for prediction. The collected data of RPA at A1, A2, A3, and A4 during the validation period are $0.14g$, $0.12g$, $0.09g$, and $0.08g$, respectively. Due to the time gap between the mainshock and aftershock, it is possible to continuously update the distribution of maximum shear modulus based on seismic response data collected at each stage.

In the inverse analysis using the proposed approach, the number of samples for each layer in the subset simulation is set to $N_l = 500$, and the initial conditional probability is set to $p_0 = 0.1$. Figure 16 illustrates the convergence process of the proposed model updating approach for calibration period. It can be observed that after 500 iterations, the RPA value has converged to $0.28g$, consistent with the experimental record data at A1, demonstrating the validity of the calculations. In addition, utilizing RPA data allows for the real-time updating of low-dimensional K-L random variables. Based on the posterior samples of low-dimensional random variables,

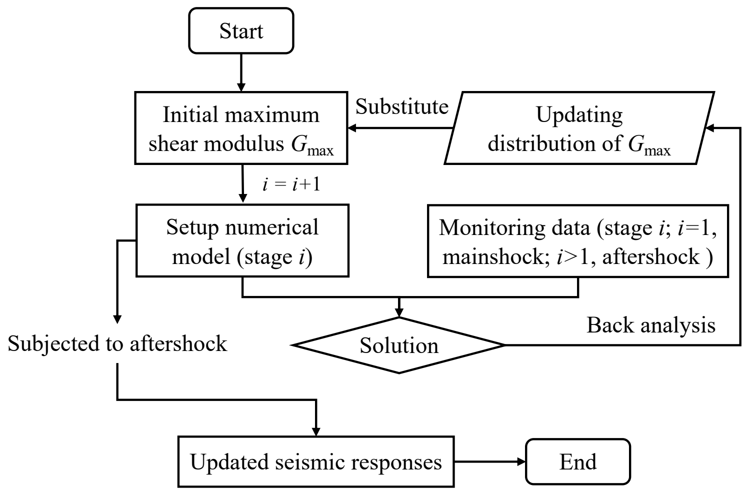

Figure 15: Illustration of slope multi-stage inverse analysis.

the posterior distribution of $G_{\max}$ at various points in space is obtained, as shown in Figure 17. Based on this distribution of $G_{\max}$, conducting aftershock analysis under an IPA of $0.08g$ yields a PGA result of $0.13g$ at point A1. Comparing this with the RPA value collected by accelerometers, which is $0.14g$, it can be concluded that the predictive accuracy of the proposed approach reaches 93%. When compared to the typical random field in Figure 8, after considering real-site response data, there is a noticeable reduction in the posterior standard deviations of the parameters, reflecting a decrease in parameter uncertainty. Furthermore, the results of the $G_{\max}$ parameter inversion vary across different locations in space, which is due to the varying influence of the soil at different locations on the acceleration response. In addition, there are more significant changes in the mean values of the $G_{\max}$ for the soil near the data collection points compared to the prior mean values. This demonstrates the necessity to consider material spatial variability in stochastic analyses, highlighting limitations in traditional deterministic inverse analysis methods or probabilistic inverse analysis methods that treat parameters as random variables.

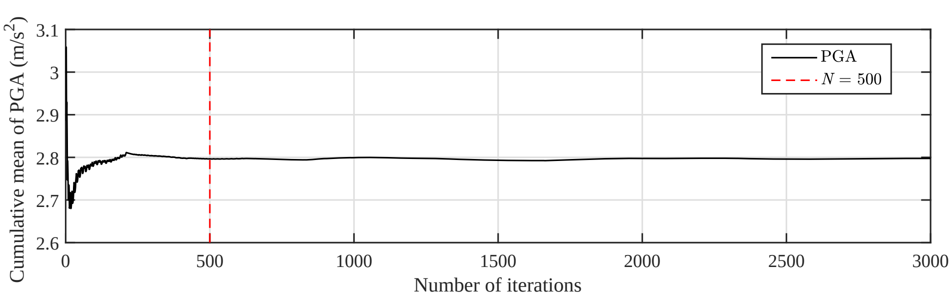

Figure 16: Convergence process at A1 of proposed model updating approach.

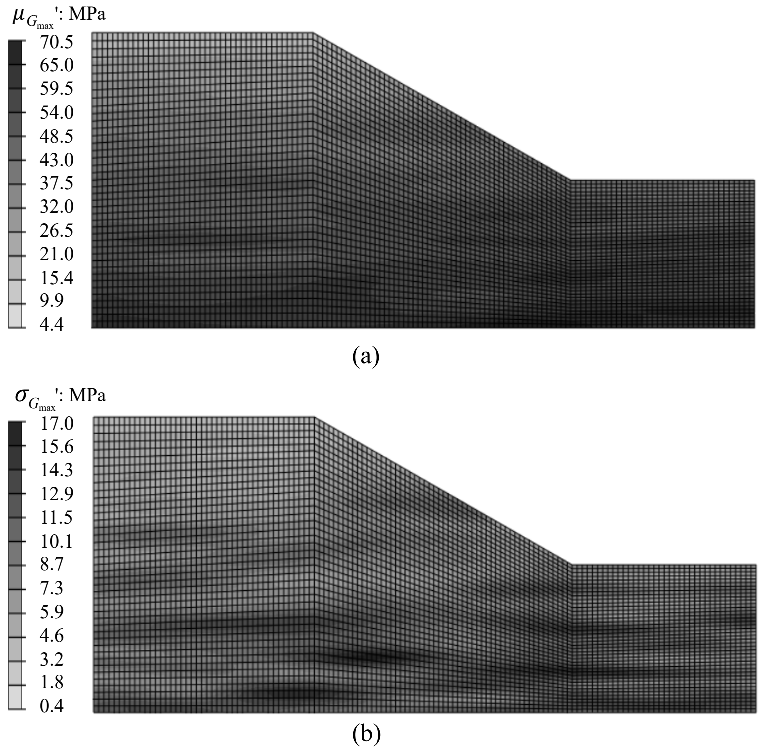

Figure 17: Posterior means and standard deviations for maximum shear modulus $G_{\max}$ of all variables via model updating approach. (a) Posterior means; (b) posterior standard deviations.

6. Conclusions

In this paper, a shaking table experimental test is first carried out, in which a slope dynamic system is investigated. Then, a stochastic model updating approach for slope seismic analysis combining subset simulations with adaptive Bayesian updating with structural reliability methods and dimensionality reduction of K-L expansion is proposed. The approach aims at updating the spatial distribution of soils for predicting the seismic response of slopes. In addition, by acquiring data from shaking table experiments, the numerical implementation of model updating approach is presented to demonstrate the implementation of this approach, showcasing its effectiveness and feasibility. The conclusions are summarized as follows.

First, pertinent experimental shaking table test results show that PGA at all monitor positions in the clay slope increased accordingly with the increments of loading intensities. Further, the acceleration increases non-linearly with the depth of the strata. In the lower sections with shallower depths, the acceleration is relatively lower, whereas at higher elevations, the amplification effect becomes more pronounced. This observation indicates that the shear modulus of the soil exhibits spatial variability and is associated with depth.

From the seismic evolution of acceleration response and pressure response obtained by experimental results, regarding the assessment of various input ground motion types, the IQR value of PLGM is roughly 2.30 times greater than that of NPGM. That is, PLGMs carry higher and more concentrated energy, resulting in a more severe detrimental impact on slope structures, especially on the topsoil layer compared to NPGMs.

On the basis of the proposed approach, the seismic response of a slope subjected to earthquake sequence could be predicted and the uncertainty caused by spatial variability of shear modulus can be well considered and updated. Further, by acquiring data from shaking table tests, an illustrative example of a slope model is given to demonstrate the feasibility of the proposed approach. Regarding the prediction of peak acceleration response, the proposed approach achieves a predictive accuracy of 93%. The results indicate that the proposed approach is a promising and reliable method for predicting seismic response for dynamic systems.

Acknowledgements

This research is supported by the International Science and Technology Cooperation Program of Guangdong Province (Grant No. 2022A0505050047), the National Natural Science Foundation of China (Grant No. U22A20596) and the Natural Science Foundation Innovation Group Project of Hubei Province, China (Grant No. 2023AFA017). Ruohan Wang has received financial support from China Scholarship Council (CSC No. 202206270125).

Conflicts of interest

The authors declare no conflict of interest.

References

1. Nadukuru SS, Michalowski RL. Three-dimensional displacement analysis of slopes subjected to seismic loads. *Canadian Geotechnical Journal.* 2013;50(6):650–661.

2. Tsai CC, Hwang YW, Lu CC. Liquefaction, building settlement, and residual strength of two residential areas during the 2016 southern Taiwan earthquake. *Acta Geotechnica.* 2020;15:1363–1379.

3. Zhao L, Huang Y, Hu H. Stochastic seismic response of a slope based on large-scale shaking-table tests. *Engineering Geology.* 2020;277:105782.

4. Zhang S, Wang G, Sa W. Damage evaluation of concrete gravity dams under mainshock–aftershock seismic sequences. *Soil Dynamics and Earthquake Engineering.* 2013;50:16–27.

5. Zhai CH, Wen WP, Li S, Chen Z, Chang Z, Xie LL. The damage investigation of inelastic SDOF structure under the mainshock–aftershock sequence-type ground motions. *Soil Dynamics and Earthquake Engineering.* 2014;59:30–41.

6. Luo Q, He M, Chen F, Li Z. Probabilistic seismic performance assessment of timber-steel hybrid structures subjected to mainshock-aftershock sequences. *Soil Dynamics and Earthquake Engineering.* 2021;141:106532.

7. Wen W, Ji D, Zhai C, Li X, Sun P. Damage spectra of the mainshock-aftershock ground motions at soft soil sites. *Soil Dynamics and Earthquake Engineering.* 2018;115:815–825.

8. Bai Y, Ma Y, Yang Q, Florez-Lopez J, Li X, Biondini F. Earthquake-induced damage updating for remaining-life assessment of steel frame substructure systems. *Mechanical Systems and Signal Processing.* 2021;159:107782.

9. Somerville PG, Smith NF, Graves RW, Abrahamson NA. Modification of empirical strong ground motion attenuation relations to include the amplitude and duration effects of rupture directivity. *Seismological Research Letters.* 1997;68(1):199–222.

10. Baker JW. Quantitative classification of near-fault ground motions using wavelet analysis. *Bulletin of the Seismological Society of America.* 2007;97(5):1486–1501.

11. Mavroeidis GP, Papageorgiou AS. A mathematical representation of near-fault ground motions. *Bulletin of the Seismological Society of America.* 2003;93(3):1099–1131.

12. Chen G, Yang J, Wang R, Li K, Liu Y, Beer M. Seismic damage analysis due to near-fault multipulse ground motion. *Earthquake Engineering & Structural Dynamics.* 2023;52(15):5099–5116.

13. Wang R, Li S, Liu Y, Hu X, Lai X, Beer M. Peridynamics-based large-deformation simulations for near-fault landslides considering soil uncertainty. *Computers and Geotechnics.* 2024.

14. Bao Y, Huang Y, Zhu C. Effects of near-fault ground motions on dynamic response of slopes based on shaking table model tests. *Soil Dynamics and Earthquake Engineering.* 2021;149:106869.

15. Bao Y, Hu H, Gan G. Seismic response analysis of slope reinforced by pile-anchor structures under near-fault pulse-like ground motions. *Soil Dynamics and Earthquake Engineering.* 2023;164:107576.

16. Zheng Z, Yufeng G, Fei Z, Jian S, Degao Z. Effects of soil dynamic response on post-earthquake deformation of slopes based on nested Newmark model. *Earthquake Engineering and Engineering Vibration.* 2020;19:573–582.

17. Mircevska V, Nastev M, Nanevska A. Seismic slope displacement of tailings dam: a comparative study between Modified Newmark and Mohr-Coulomb Models. *Journal of Earthquake Engineering.* 2022;26(15):7878–7900.

18. Zhang Y, Liu J, Cheng Q, et al. A new permanent displacement model considering pulse-like ground motions and its application in landslide hazard assessment. *Soil Dynamics and Earthquake Engineering.* 2022;163:107556.

19. Jibson RW. Methods for assessing the stability of slopes during earthquakes—A retrospective. *Engineering Geology.* 2011;122(1-2):43–50.

20. Pang R, Xu B, Zhou Y, Song L. Seismic time-history response and system reliability analysis of slopes considering uncertainty of multi-parameters and earthquake excitations. *Computers and Geotechnics.* 2021;136:104245.

21. Yiğit A. Prediction of amount of earthquake-induced slope displacement by using Newmark method. *Engineering Geology.* 2020;264:105385.

22. Wang R, Li D, Chen EJ, Liu Y. Dynamic prediction of mechanized shield tunneling performance. *Automation in Construction.* 2021;132:103958.

23. Chen X, Hu Y, Zhang L, Liu Y. 3D large-deformation modelling on face instability and sinkhole formation during tunnelling through non-uniform soils. *Tunnelling and Underground Space Technology.* 2023;134:105011.

24. Wang R, Li DQ, Wang MY, Liu Y. Deterministic and probabilistic investigations of piping occurrence during tunneling through spatially variable soils. *ASCE-ASME Journal of Risk and Uncertainty in Engineering Systems, Part A: Civil Engineering.* 2021;7(2):04021009.

25. Wang R, Sun PG, Li DQ, Tyagi A, Liu Y. Three-dimensional seepage investigation of riverside tunnel construction considering heterogeneous permeability. *ASCE-ASME Journal of Risk and Uncertainty in Engineering Systems, Part A: Civil Engineering.* 2021;7(4):04021041.

26. He L, Liu Y, Bi S, Wang L, Broggi M, Beer M. Estimation of failure probability in braced excavation using Bayesian networks with integrated model updating. *Underground Space.* 2020;5(4):315–323.

27. Ouyang JY, Liu Y, Yao K, Yang CJ, Niu HF. Model Updating of Slope Stability Analysis Using 3D Conditional Random Fields. *ASCE-ASME Journal of Risk and Uncertainty in Engineering Systems, Part A: Civil Engineering.* 2021;7(3):04021034.

28. Ouyang JY, Liu Y. Model updating for slope stability assessment in spatially varying soil parameters using multi-type observations. *Mechanical Systems and Signal Processing.* 2022;171:108906.

29. Biswal S, Ramaswamy A. Finite element model updating of concrete structures based on imprecise probability. *Mechanical Systems and Signal Processing.* 2017;94:165–179.

30. DiazDelaO F, Garbuno-Inigo A, Au S, Yoshida I. Bayesian updating and model class selection with subset simulation. *Computer Methods in Applied Mechanics and Engineering.* 2017;317:1102–1121.

31. Lye A, Cicirello A, Patelli E. Sampling methods for solving Bayesian model updating problems: A tutorial. *Mechanical Systems and Signal Processing.* 2021;159:107760.

32. Bayesian inference of random fields represented with the Karhunen–Loève expansion. *Computer Methods in Applied Mechanics and Engineering.* 2020;358:112632.

33. Liu Y, Li L, Chang Z. Efficient Bayesian model updating for dynamic systems. *Reliability Engineering & System Safety.* 2023;236:109294.

34. Jiang SH, Wang L, Ouyang S, Huang J, Liu Y. A comparative study of Bayesian inverse analyses of spatially varying soil parameters for slope reliability updating. *Georisk: Assessment and Management of Risk for Engineered Systems and Geohazards.* 2022;16(4):746–765.

35. Jiang SH, Huang J, Qi XH, Zhou CB. Efficient probabilistic back analysis of spatially varying soil parameters for slope reliability assessment. *Engineering Geology.* 2020;271:105597.

36. Luo J, Pei X, Evans SG, Huang R. Mechanics of the earthquake-induced Hongshiyan landslide in the 2014 Mw 6.2 Ludian earthquake, Yunnan, China. *Engineering Geology.* 2019;251:197–213.

37. Maejima Y, Nagatsuka S, Higashi T. Mineralogical composition of iron oxides in red-and yellow-colored soils from Southern Japan and Yunnan, China. *Soil Science and Plant Nutrition.* 2000;46(3):571–580.

38. Ma S, Huang M, Hu P, Yang C. Soil-water characteristics and shear strength in constant water content triaxial tests on Yunnan red clay. *Journal of Central South University.* 2013;20(5):1412–1419.

39. Shein E. The particle-size distribution in soils: problems of the methods of study, interpretation of the results, and classification. *Eurasian Soil Science.* 2009;42(3):284–291.

40. Yang F, Zhang GL, Yang F, Yang RM. Pedogenetic interpretations of particle-size distribution curves for an alpine environment. *Geoderma.* 2016;282:9–15.

41. To P, Scheuermann A, Williams D. Quick assessment on susceptibility to suffusion of continuously graded soils by curvature of particle size distribution. *Acta Geotechnica.* 2018;13(5):1241–1248.

42. Turan A, Hinchberger SD, El Naggar H. Design and commissioning of a laminar soil container for use on small shaking tables. *Soil Dynamics and Earthquake Engineering.* 2009;29(2):404–414.

43. Pu X, Wan L, Wang P. Initiation mechanism of mudflow-like loess landslide induced by the combined effect of earthquakes and rainfall. *Natural Hazards.* 2021;105(3):3079–3097.

44. Ancheta TD, Darragh RB, Stewart JP, et al. NGA-West2 Database. *Earthquake Spectra.* 2014;30(3):989-1005.

45. Cao Z, Wang Y, Li D. Quantification of prior knowledge in geotechnical site characterization. *Engineering Geology.* 2016;203:107–116.

46. Shinozuka M, Deodatis G. Simulation of multi-dimensional Gaussian stochastic fields by spectral representation. *Applied Mechanics Review.* 1996.

47. Montoya-Noguera S, Zhao T, Hu Y, Wang Y, Phoon KK. Simulation of non-stationary non-Gaussian random fields from sparse measurements using Bayesian compressive sampling and Karhunen-Loève expansion. *Structural Safety.* 2019;79:66–79.

48. Li CC, Der Kiureghian A. Optimal discretization of random fields. *Journal of Engineering Mechanics.* 1993;119(6):1136–1154.

49. Liu Y, Lee FH, Quek ST, Beer M. Modified linear estimation method for generating multi-dimensional multi-variate Gaussian field in modelling material properties. *Probabilistic Engineering Mechanics.* 2014;38:42–53.

50. Papaioannou I, Betz W, Zwirglmaier K, Straub D. MCMC algorithms for subset simulation. *Probabilistic Engineering Mechanics.* 2015;41:89–103.

51. Betz W, Papaioannou I, Beck JL, Straub D. Bayesian inference with subset simulation: strategies and improvements. *Computer Methods in Applied Mechanics and Engineering.* 2018;331:72–93.

52. Banerjee S, Goh S, Lee F. Earthquake-induced bending moment in fixed-head piles in soft clay. *Géotechnique.* 2014;64(6):431–446.

53. Liu Y, Zhang L. Seismic response of pile–raft system embedded in spatially random clay. *Géotechnique.* 2019;69(7):638–645.

54. Chen G, Liu Y, Beer M. Effects of response spectrum of pulse-like ground motion on stochastic seismic response of tunnel. *Engineering Structures.* 2023;289:116274.

55. Chong P. *Characterization of Singapore lower marine clay.* PhD thesis. National University of Singapore, Singapore 2002.

56. Zhang L, Goh S, Yi J. A centrifuge study of the seismic response of pile–raft systems embedded in soft clay. *Géotechnique.* 2017;67(6):479–490.

57. Schevenels M, Lombaert G, Degrande G, Degrauwe D, Schoors B. The Green's functions of a vertically inhomogeneous soil with a random dynamic shear modulus. *Probabilistic Engineering Mechanics.* 2007;22(1):100–111.

58. Ayad F, Bekkouche A, Houmadi Y. Effect of the spatial variation of the shear modulus on soil liquefaction potential. *Electronic Journal of Geotechnical Engineering.* 2012;17:3281–3289.

59. Phoon KK, Kulhawy FH. Evaluation of geotechnical property variability. *Canadian Geotechnical Journal.* 1999;36(4):625–639.

60. Ching J, Phoon KK. Effect of element sizes in random field finite element simulations of soil shear strength. *Computers & Structures.* 2013;126:120–134.

61. Chen J, Wang L, Pu X, Li F, Li T. Experimental study on the dynamic characteristics of low-angle loess slope under the influence of long-and short-term effects of rainfall before earthquake. *Engineering Geology.* 2020;273:105684.